

Tunable working bandwidth terahertz switch based on magnetic valley photonic crystal

Mingxia Hou(侯铭霞), Hongming Fei(费宏明), Han Lin(林瀚), and Mingda Zhang(张明达)
Citation: Chin. Phys. B, 2025, 34 (**5**): 058702. DOI: 10.1088/1674-1056/adbb5b
http://cpb.iphy.ac.cn; http://iopscience.iop.org/cpb

What follows is a list of articles you may be interested in

Topological slow light and rainbow trapping of surface wave in valley photonic crystal bounded by air

Shuheng Chen(陈书恒), Yi Qi(齐奕), Yucen Li(李昱岑), Qihao Wang(王琪皓), and Yuanjiang Xiang(项元江)
Chin. Phys. B, 2024, 33 (**11**): 118701. DOI: 10.1088/1674-1056/ad7fd2

Terahertz toroidal dipole metamaterial sensors for detection of aflatoxin B1

Jianwei Xu(徐建伟), Shoujian Ouyang(欧阳收剑), Shouxin Duan(段守鑫), Liner Zou(邹林儿), Danni Ye(叶丹妮), Sijia Yang(杨思嘉), and Xiaohua Deng(邓晓华)
Chin. Phys. B, 2024, 33 (**3**): 038701. DOI: 10.1088/1674-1056/acef02

Electron beam pumping improves the conversion efficiency of low-frequency photons radiated by perovskite quantum dots

Peng Du(杜鹏), Yining Mu(母一宁), Hang Ren(任航), Idelfonso Tafur Monroy, Yan-Zheng Li(李彦正), Hai-Bo Fan(樊海波), Shuai Wang(王帅), Makram Ibrahim, and Dong Liang(梁栋)
Chin. Phys. B, 2023, 32 (**4**): 048704. DOI: 10.1088/1674-1056/ac8348

Super-resolution reconstruction algorithm for terahertz imaging below diffraction limit

Ying Wang(王莹), Feng Qi(祁峰), Zi-Xu Zhang(张子旭), and Jin-Kuan Wang(汪晋宽)
Chin. Phys. B, 2023, 32 (**3**): 038702. DOI: 10.1088/1674-1056/aca9c7

Ultra-compact terahertz switch with graphene ring resonators

Jian-Zhong Sun(孙建忠), Le Zhang(章乐), Fei Gao(高飞)
Chin. Phys. B, 2016, 25 (**10**): 108701. DOI: 10.1088/1674-1056/25/10/108701

Tunable working bandwidth terahertz switch based on magnetic valley photonic crystal

Mingxia Hou(侯铭霞)[1,3], Hongming Fei(费宏明)[1,2,3,†], Han Lin(林瀚)[4], and Mingda Zhang(张明达)[1,3]

[1] *College of Physics and Optoelectronics, Taiyuan University of Technology, Taiyuan* 030024, *China*
[2] *State Key Laboratory of Quantum Optics and Quantum Optics Devices, Shanxi University, Taiyuan* 030006, *China*
[3] *Shanxi Key Laboratory of Precision Measurement Physics, Taiyuan University of Technology, Taiyuan* 030024, *China*
[4] *Centre for Atomaterials and Nanomanufacturing, School of Science, RMIT University, Melbourne, Victoria* 3000, *Australia*

(Received 11 January 2025; revised manuscript received 20 February 2025; accepted manuscript online 28 February 2025)

Terahertz (THz) switches are essential components of THz communication systems. THz switches based on conventional waveguides and photonic crystal structures are sensitive to manufacturing defects and sharp bending, resulting in high scattering losses. In addition, THz switches with tunable working bandwidths have not yet been demonstrated. Here, we design THz switches based on a topological valley photonic crystal (VPC) structure using magnetic materials, which can achieve high forward transmittance based on the unique spin–valley locking effect. The broad working bandwidth allows selective turning on and off at a designed wavelength region by controlling the applied magnetic field. The designed THz switch can achieve an extinction ratio of up to 31.66 dB with an insertion loss of less than 0.13 dB. The 3-dB bandwidth is up to 49 GHz. This tunable THz switch can be experimentally fabricated by current fabrication techniques and thus can find broad applications in THz communication systems.

Keywords: terahertz switch, magnetic material, valley photonic crystal, tunable bandwidth

PACS: 87.50.U–, 85.70.Ay, 42.70.Qs, 78.67.Pt

DOI: 10.1088/1674-1056/adbb5b **CSTR:** 32038.14.CPB.adbb5b

1. Introduction

Terahertz (THz) waves are generally referred to as electromagnetic waves with operating wavelengths between 30 μm and 3 mm (with a frequency range of 0.1–10 THz), which are located at the intersection of the microwave and infrared bands in the electromagnetic spectrum. This special location gives it many different characteristics from other electromagnetic waves. In recent years, THz technology has had a wide range of application prospects in communications,[1–4] imaging,[5,6] spectroscopy,[7] security,[8] military defense,[9] etc. Among them, THz communication has great potential and can provide a higher rate and larger bandwidth than 5G, which is the key to developing a 6G mobile communication network. THz technology can be used to solve long-standing interconnection problems,[2] thus realizing the "Internet of things". In order to realize next-generation communication systems for 6G and beyond, high-capacity communication needs to be realized by integrating compact, low-power devices such as waveguides, switches and modulators. In particular, on-chip THz switches can be easily integrated into terahertz interconnect communication systems, allowing active control of the data transmission channels,[10] which have attracted great attention.

A variety of on-chip integrated THz switches have been demonstrated, including switches based on metallic waveguide structures,[11,12] photonic crystal (PC) waveguides,[10,13–17] ring resonator structures,[18–20] plasmonic structures,[21,22] layered photonic structures,[23] etc. Compared to other on-chip integrated THz switches, THz switches based on PC waveguide structures[24–31] using magnetic materials feature high design flexibility, miniaturization and low power consumption.[13–15,17] However, conventional magnetic PC structures have low transmission efficiency due to high scattering losses caused by defects and sharp bends. In comparison, topological valley photonic crystal (VPC) structures based on the spin–valley locking effect can realize robust unidirectional optical transmission and achieve high forward transmittance close to unity.[2,10,32–38] THz switches based on the VPC structure of silicon materials have been demonstrated to work by pumping high-intensity external light. This working principle is sensitive to the linearity, position, angle and intensity of the externally pumped light source,[10] making it a challenge to control in real applications. In comparison, THz switches based on the magnetic PC structures[13–15,17] can be easily controlled by applying an external magnetic field and have a fast response time for broad applications.[14,15] High-performance functional devices based on VPC structures of different materials have been demonstrated at different operating wavelengths.[39–45] However, there has been no demonstration of VPC structures based on magnetic materials working in the THz region, particularly for switching

[†]Corresponding author. E-mail: feihongming@tyut.edu.cn

© 2025 Chinese Physical Society and IOP Publishing Ltd. All rights, including for text and data mining, AI training, and similar technologies, are reserved.

applications.

In this paper, we demonstrate the design of THz switches based on VPC structures using LuBiIG single-crystal ferrite material, which can achieve high forward transmittance based on the unique spin–valley locking effect. In addition, the switching bandwidth can be tuned by the strength of the external magnetic field for the first time. The designed THz switches can achieve an extinction ratio of up to 31.66 dB with an insertion loss of less than 0.13 dB. The 3-dB operating bandwidth is up to 49 GHz. The turn-on time is 36 ps. In addition, the design meets experimental fabrication requirements. Thus, it will find broad applications in THz communications and the design principle can be generally applied to design other integrated THz devices.

2. Design of magnetic valley photonic crystal structures

The conceptual demonstration of the THz switch based on a VPC structure made of LuBiIG single-crystal ferrite material is shown in Fig. 1(a). The structure is a topological waveguide consisting of two mirror-symmetric VPC structures, namely, VPC1 and VPC2. The THz wave propagates through the waveguide along the x-direction. Meanwhile, the magnetic field is applied along the y-direction, perpendicular to the propagation direction of THz waves. When there is no external magnetic field, the THz waves within the working bandwidth can pass through the waveguide with a high transmittance, which is considered the "on" state [Fig. 1(b)]. In comparison, a certain range (f_1) within the bandwidth can be turned off when an external magnetic field is applied [Figs. 1(c) and 1(d)]. By further increasing the strength of the magnetic field, the turn-off wavelength range can be shifted to a high frequency (f_2) [Figs. 1(e) and 1(f)]. In this way, the turn-off wavelength range can be flexibly controlled by the strength of the external magnetic field. The finite-difference time-domain (FDTD) simulation information of the terahertz switch based on magnetic VPC is shown in supplement 1 Section 1.

LuBiIG single-crystal ferrite material with thickness $d = 190$ μm is chosen in this study (simulated in three dimensions (3D) for FDTD simulations as shown in supplement 1 Section 2), which is suitable for designing a high transmission waveguide in the terahertz region according to its refractive index.[46] Thus, combined with the ease of production of ferrite materials at a low cost, ferrite is a promising material in the terahertz region. LuBiIG is a gyromagnetic ferrite material (detailed information about the experimental schemes can be found in the supplement 1 Section 3) whose permeability tensor is given by the literature[47]

$$[\mu] = \begin{bmatrix} \mu & 0 & -\mathrm{j}\kappa \\ 0 & \mu_0 & 0 \\ \mathrm{j}\kappa & 0 & \mu \end{bmatrix}. \tag{1}$$

The matrix elements of the permeability tensor are given by the following equation:

$$\mu = \mu_0 \left(1 + \frac{\omega_{\mathrm{ex}}\omega_{\mathrm{m}}}{\omega_{\mathrm{ex}}^2 - \omega^2}\right), \tag{2a}$$

$$\kappa = \mu_0 \frac{\omega\omega_{\mathrm{m}}}{\omega_{\mathrm{ex}}^2 - \omega^2}, \tag{2b}$$

where $\omega_{\mathrm{ex}} = \gamma B_{\mathrm{ex}}$, $\omega_{\mathrm{m}} = \mu_0\gamma M_{\mathrm{s}}$, γ is the gyromagnetic ratio of 1.758×10^{11} rad·T^{-1}·s^{-1}, μ_0 is the permeability in vacuum, ω is the circular frequency of the incident wave, B_{ex} is the magnetic induction of the external magnetic field, M_{s} is the saturation magnetization of ferrite materials. Considering ferromagnetic loss, ω_{ex} should be replaced by $\omega_{\mathrm{ex}} + \mathrm{j}\mu_0\gamma\Delta H/2$. LuBiIG has a dielectric constant of 4.85, a saturation magnetization of 1560 G and the ferromagnetic resonance linewidth $2\Delta H$ of LuBiIG is 5.1 Oe. Here, the magnetic field is applied along the y-direction perpendicular to the direction of the waveguide as transverse electric (TE) modes are used.[48] Therefore, for TE modes,[48]

$$\mu_{\mathrm{TE}} = \frac{\mu^2 - \kappa^2}{\mu} = \mu_0 \frac{(\omega_{\mathrm{ex}} + \omega_{\mathrm{m}})^2 - \omega^2}{\omega_{\mathrm{ex}}(\omega_{\mathrm{ex}} + \omega_{\mathrm{m}}) - \omega^2}, \tag{3}$$

when no external magnetic field is applied, the dispersion curves of LuBiIG in the THz band are shown in Figs. S6(a) and S6(b), respectively.

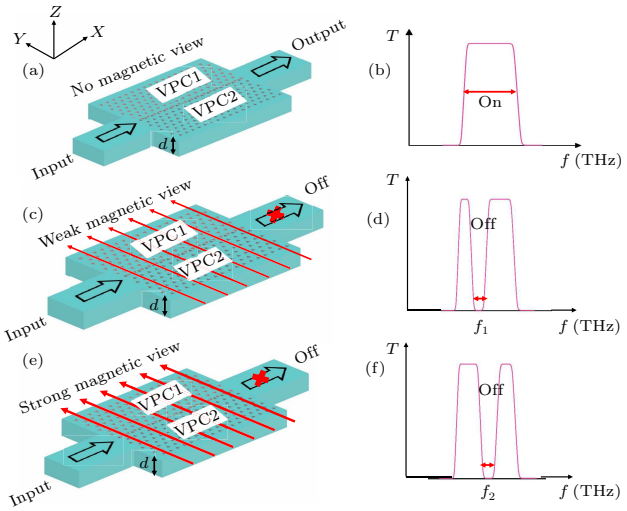


Fig. 1. Conceptual demonstration of a magnetically tunable THz switch based on VPC structures. (a) Three-dimensional schematic of the THz switch. (b) Schematic plot of forward transmittance spectrum at the on-state. (c) Conceptual demonstration of turning off an optical switch by applying a weak magnetic field. (d) The corresponding forward transmittance spectrum with a region being turned off. (e) Conceptual demonstration of turning off a different wavelength range by applying a stronger magnetic field. (f) The corresponding forward transmittance spectrum with a different region being turned off.

The design process starts with designing a honeycomb lattice PC structure (the lattice constant $a = 242.5$ μm) with a Dirac cone in its photonic band structure [pink curve in Fig. 2(b)], which has triangular air holes $r_A = r_B = 48$ μm (r is defined as the distance between the triangular vertices and the geometric center [Fig. 2(a)]). Therefore, the structure has

C_{6v} rotational symmetry. Here, we use commercial 3D FDTD software (Lumerical FDTD Solutions) to calculate the band structure.

The minimum band model of bulk dispersions resorting to the photonic effective Hamiltonian through the $k \cdot p$ approximation can be expressed as

$$\hat{H} = v_{\mathrm{D}} \left(\hat{\sigma}_x \hat{\tau}_z \delta k_x + \hat{\sigma}_y \delta k_y \right) + \lambda_{\varepsilon_{\mathrm{r}}}^{\mathrm{P}} \hat{\sigma}_z, \tag{4}$$

where v_{D} is the group velocity. $\hat{\sigma}_i$ and $\hat{\tau}_j$ are the Pauli matrices acting on sublattice and valley spaces, respectively. $\delta \boldsymbol{k}$ measures from the valley center K or K' point. In the perturbation term $\lambda_{\varepsilon_{\mathrm{r}}}^{\mathrm{P}} \hat{\sigma}_z$, $\lambda_{\varepsilon_{\mathrm{r}}}^{\mathrm{P}}$ is zero considering space and time inversion symmetry, which also corresponds to zero perturbation in the initial structure. Due to the change of the size of air holes, the spatial inversion symmetry is broken and a bandgap with a width of $2\left|\lambda_{\varepsilon_{\mathrm{r}}}^{\mathrm{P}}\right|$ is opened. Note that $\lambda_{\varepsilon_{\mathrm{r}}}^{\mathrm{P}}$ is proportional to the difference between the integration of ε_{r} on the two triangles A and B [Fig. 2(a)], as $\left|\lambda_{\varepsilon_{\mathrm{r}}}^{\mathrm{P}}\right| \propto \left|\int_B \varepsilon_{\mathrm{r}} \mathrm{d}s - \int_A \varepsilon_{\mathrm{r}} \mathrm{d}s\right|$, where ε_{r} is the relative permittivity. Take the VPC with $r_A = 115$ μm and $r_B = 0$ μm in Fig. 2(a) as an example, $\int_B \varepsilon_{\mathrm{r}} \mathrm{d}s < \int_A \varepsilon_{\mathrm{r}} \mathrm{d}s$ leads to $\lambda_{\varepsilon_{\mathrm{r}}}^{\mathrm{P}} < 0$ and thus a complete band gap (blue shaded area) clearly exists in Fig. 2(b), which can be achieved by changing the size of a set of the triangular air holes r_A or r_B, which degenerates the K and K' points. The maximum bandgap can be obtained (see supplement 1 Section 4) when r_A or r_B is taken to be 0 when the other is maximized.[49] As a result, $r_A = 0$ μm, $r_B = 115$ μm for VPC1, and VPC2 is the mirror-symmetric structure of VPC1, which has $r_A = 115$ μm, $r_B = 0$ μm. In this case, the C_{6v} symmetry is reduced to the C_3 symmetry. The frequency range of the band gap is 0.476–0.536 THz. Furthermore, the topological properties of VPC1 and VPC2 can be described in terms of the valley topological indices:[50,51] $C_{\tau_z} = \tau_z \mathrm{sgn}\left(\lambda_{\varepsilon_{\mathrm{r}}}^{\mathrm{P}}\right)/2$. The topological indices of the K and K' valley are $C_K = 1/2$ and $C_{K'} = -1/2$, respectively. Therefore, even if the total Chern number is 0, we can define this new nonzero topological invariant, namely, the valley Chern number[52] $C_V = C_K - C_{K'}$, which is non-zero. For VPC1 and VPC2, the valley Chern numbers are 1 and −1, respectively. According to the body boundary correspondence,[53] a topological phase transition will occur when the topological number at the interface changes. The number of edge states in each valley is determined by the difference between the valley topological index across the interface, which is given by $\Delta C_{K/K'} = \left|C_{K/K'}^{\mathrm{VPC1}} - C_{K/K'}^{\mathrm{VPC2}}\right| = 1$. Therefore, topological edge states with a spin–valley locking effect can be obtained by constructing boundaries using VPCs (VPC1 and VPC2) with different Chern numbers. Here, VPC1 and VPC2 can

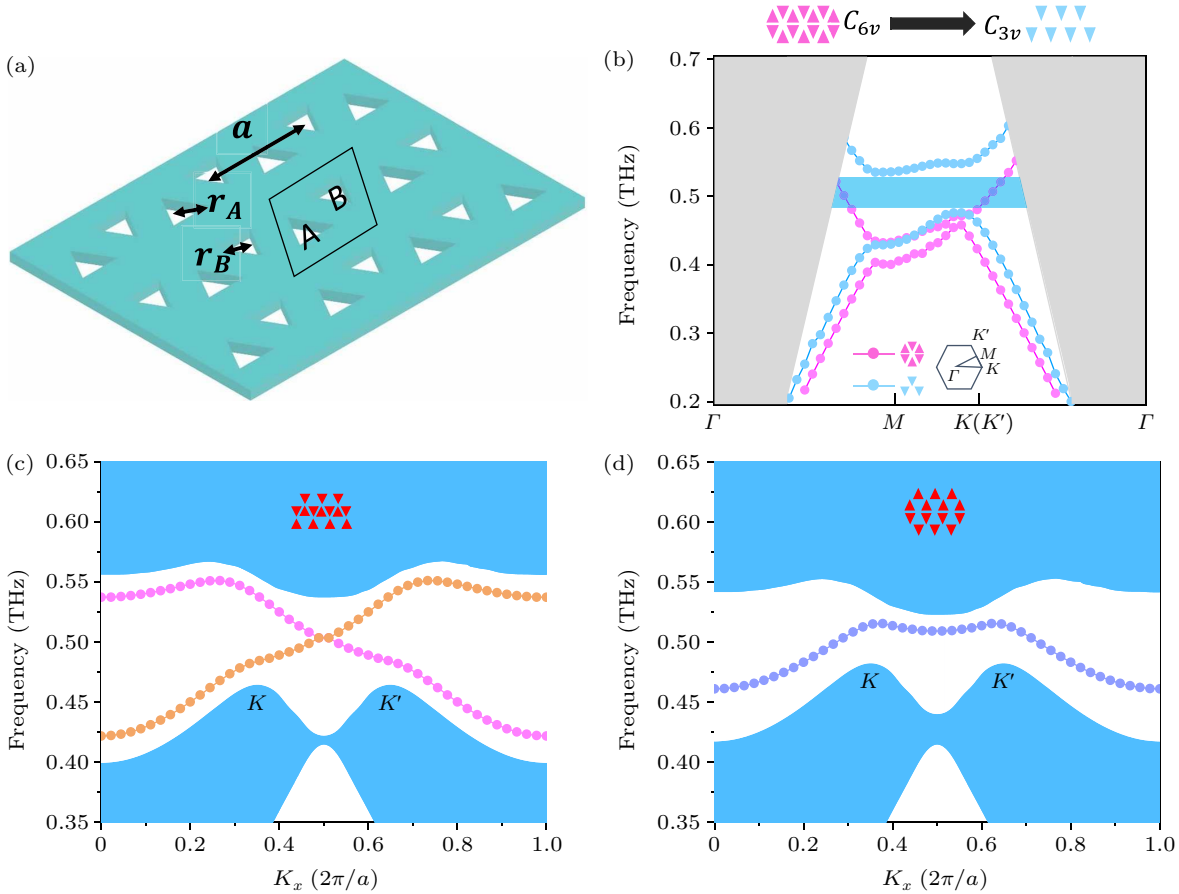


Fig. 2. (a) Schematic diagram of the VPC structure based on LuBiIG material. (b) Photonic band diagrams of the initial honeycomb lattice PC (pink dotted solid line) and the VPC structure (blue dotted solid line). The gray-shaded region is the light cone, and the blue-shaded region is the photonic bandgap. The band diagrams of the edge state for the (c) zigzag and (d) beard-type boundaries.

be combined to form two different types of edge state waveguide structures, zigzag and beard types, whose edge state band diagrams are shown in Figs. 2(c) and 2(d), respectively. Compared with the beard-type structure, the zigzag-type structure has a high transmittance close to unity and a wide bandwidth[54] across the entire topological bandgap [Fig. S5(c)] due to the strong spin–valley locking effect leading to different polarizations being locked to K or K' valleys (see supplement 1 Section 6). Therefore, a zigzag-type boundary structure is chosen in this study.

We combine VPC1 and VPC2 to form a straight waveguide [Fig. 3(a)], a Z-shape waveguide [Fig. 3(b)] and an Ω-shape waveguide [Fig. 3(c)], respectively, and the top layer of each figure shows the corresponding electric field intensity distributions at the frequency of 0.5 THz. The full width at half maximum, also called the 3-dB bandwidth, defines the working bandwidth. The forward transmittance spectra of the three waveguides without a magnetic field are shown in Figs. 3(d)-3(f), which have 3-dB bandwidth ranges of 567–626 μm, 570–617.8 μm and 582–613.2 μm, respectively. The highest transmittance of those three waveguides is 0.97, 0.86 and 0.83, confirming the high transmittance even with shape corners due to the spin–valley locking effect, which refers to the fact that, in VPCs, light sources with different spins (corresponding to left-handed and right-handed circularly polarized light) can be unidirectionally transported in the direction of their respective locked valleys.[52,55,56] In addition, the edge states encounter loss at the shape bends in the Z and Ω waveguides, which reduces the working bandwidth (high transmission frequency range). In summary, the high transmittance makes those waveguides ideal candidates for high-performance terahertz switches.

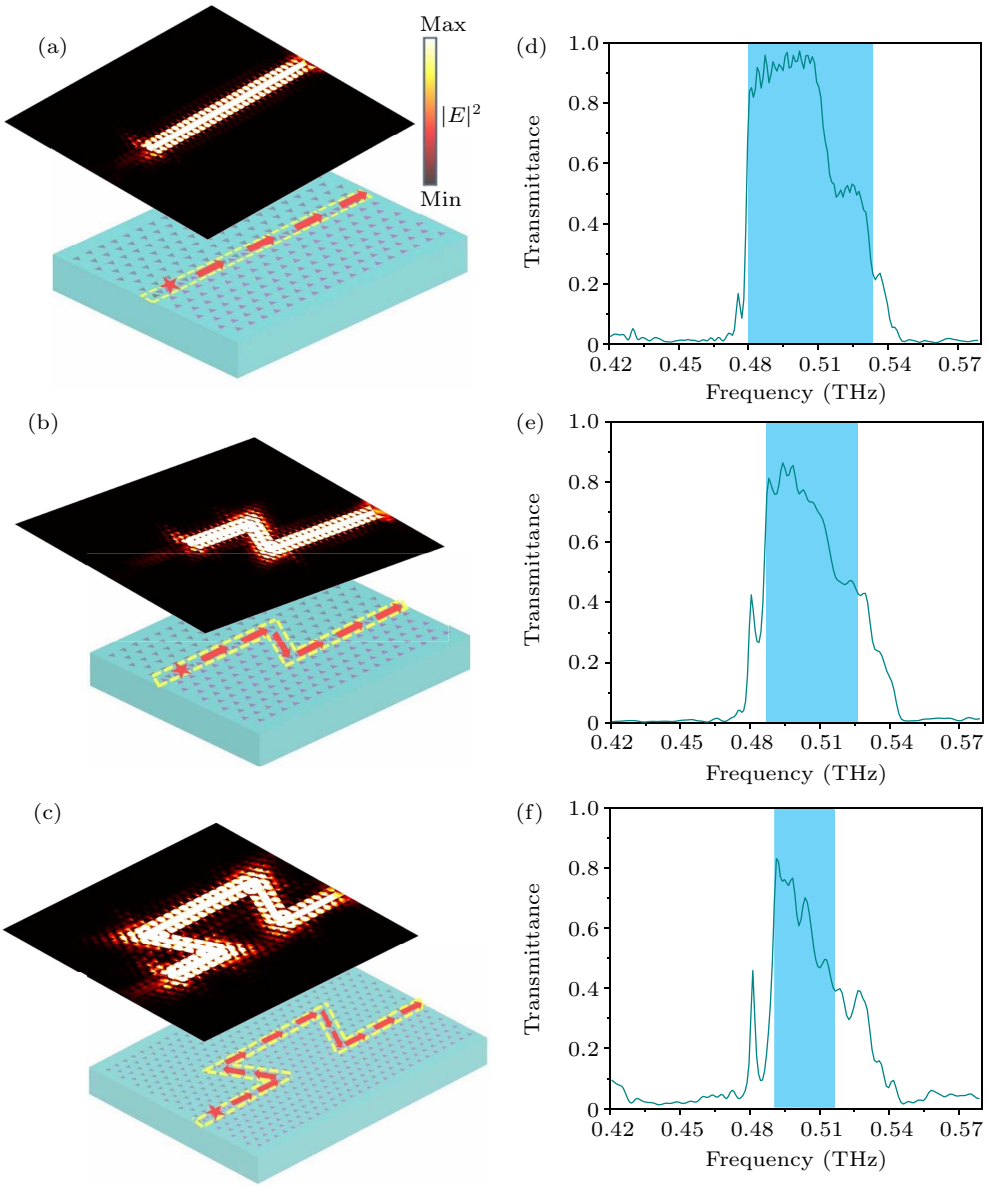


Fig. 3. Structural diagrams of (a) straight waveguide, (b) Z-waveguide, (c) Ω-waveguide, and the electric field intensity distributions at 0.5 THz frequency in the three waveguide structures in the absence of applied magnetic field. (d)–(f) Forward transmission spectra of the three waveguide structures without a magnetic field, respectively. The blue shadows mark the working bandwidths.

3. Realization of the "off" state using a magnetic field

The "off" state of the THz switch is controlled by applying an external magnetic field. By using Eq. (3), we can calculate the relationship between the magnetic permeability of the ferrite material in the frequency range of 0.42–0.58 THz. One example of applying a magnetic field of 18 T is shown in Fig. 4(a), in which one can see sharp peaks in both real and imaginary parts of the permeability. Therefore, it introduces a large refractive index in both the real and imaginary parts of the refractive index, which introduces a passband [marked by the yellow shadow in Fig. 4(b)] within the original

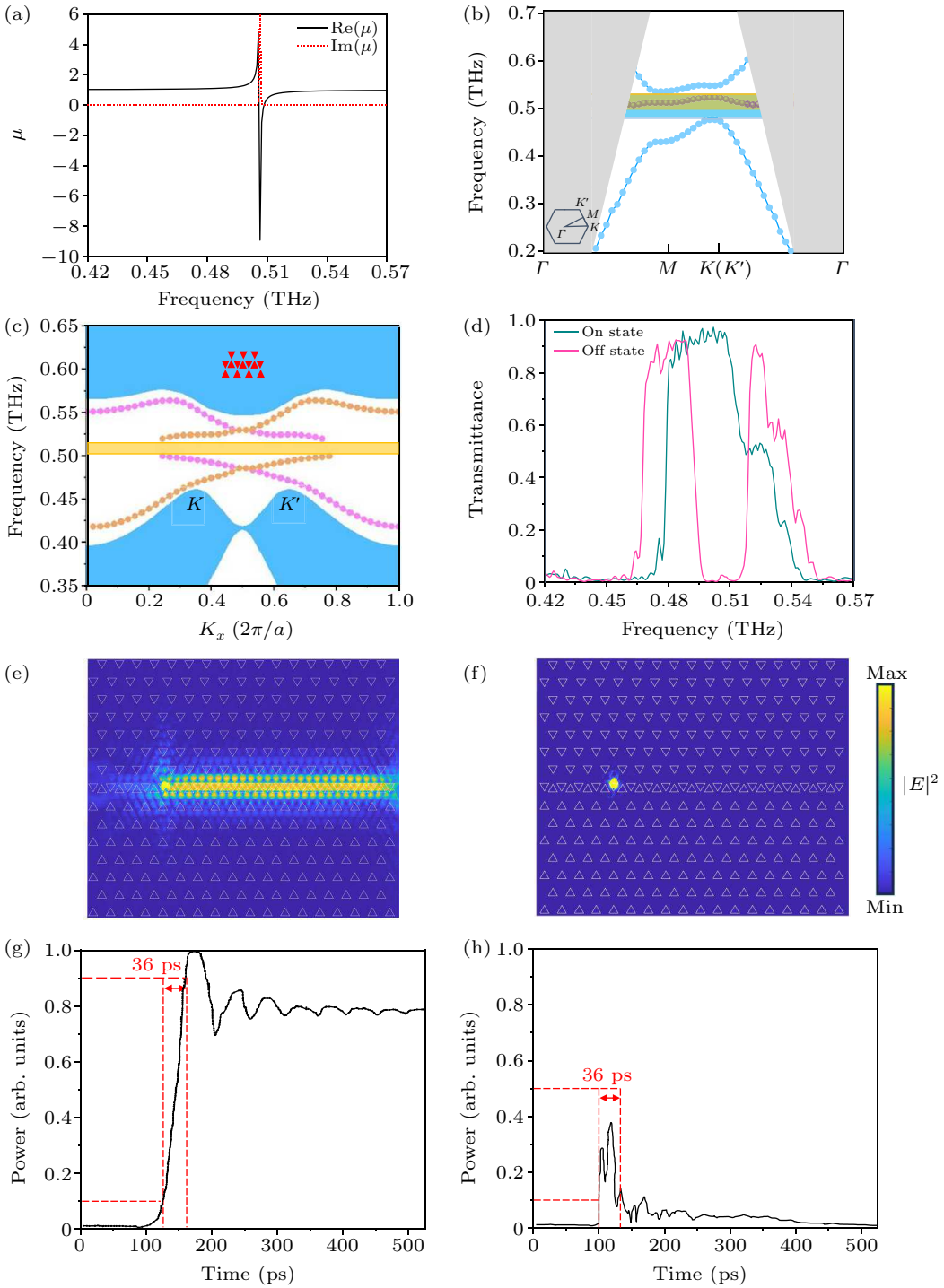


Fig. 4. (a) Magnetic permeability plot of the ferrite material with an external magnetic field of 18 T. The solid and dashed lines indicate the real and imaginary parts of the magnetic permeability, respectively. (b) Photonic bandgap diagram with an external magnetic field of 18 T. The yellow and the blue shadows mark the formed passband and the original photonic bandgap. (c) The edge state band diagram has an external magnetic field of 18 T, and the yellow shadow shows the formed gap in which no edge state exists. (d) Forward transmittance spectra of a straight waveguide structure without ("on" state, green curve) and with ("off" state, pink curve) a magnetic field of 18 T. Electric field intensity distribution at 0.5 THz in a straight waveguide structure without (e) and with (f) a magnetic field of 18 T. Time domain steady state power plots of "on" (g) and "off" (h) states.

photonic bandgap. Such a passband breaks the confinement of the optical waves in the waveguide, which dramatically reduces the transmission efficiency, resulting in a low transmittance as the "off" state. Meanwhile, the magnetic field introduces a bandgap in the edge states [marked by the yellow shadow in Fig. 4(c)], which also results in low transmittance. The combination of the two factors results in a low transmittance region (less than 0.1 in the frequency range of 0.496–0.517 THz) in the spectrum [Fig. 4(d)]. For comparison, the field intensity distributions without and with external magnetic fields at the frequency of 0.5 THz are shown in [Figs. 4(e) and 4(f)]. One can see that the THz waves can propagate through the waveguide with high efficiency when there is no external magnetic field, which can be fully turned off by using a magnetic field in the designed wavelength region. The time-domain steady-state intensity responses of the THz switch are shown in [Figs. 4(g) and 4(h)], which reach a steady state at 36 ps. The response time of the material is neglected due to the ultrafast response of the ferrite material in the THz band.

4. Tunability of the THz switch

The unique magnetic response of the ferrite material allows tuning the permeability by controlling the strength of the magnetic field [Figs. S7(a) and S7(b) in supplement 1 Section 7], resulting in different dispersion curves of refractive indices LuBiIG at terahertz bands under different magnetic fields [Figs. S8(a)–S8(d) in supplement 1 Section 8]. The resonance peak of the ferrite material gradually blueshifts with the increased strength of the magnetic field, corresponding to the position of the passband within the photonic bandgap. The calculated band diagrams at different magnetic fields (from 16.6 T to 18.9 T at a step of 0.1 T) are shown in Figs. S9(a)–S9(x) and S11(a)–S11(x) in the supplementary materials. The shifts of center frequencies of the passbands and formed stopband under external magnetic fields are plotted in Figs. S10(a) and S12(a), respectively. The trend of the blue curve is consistent with the shift of the working bandwidth shown in Figs. 5(d)–5(f). The range is defined by the potential range for shifting

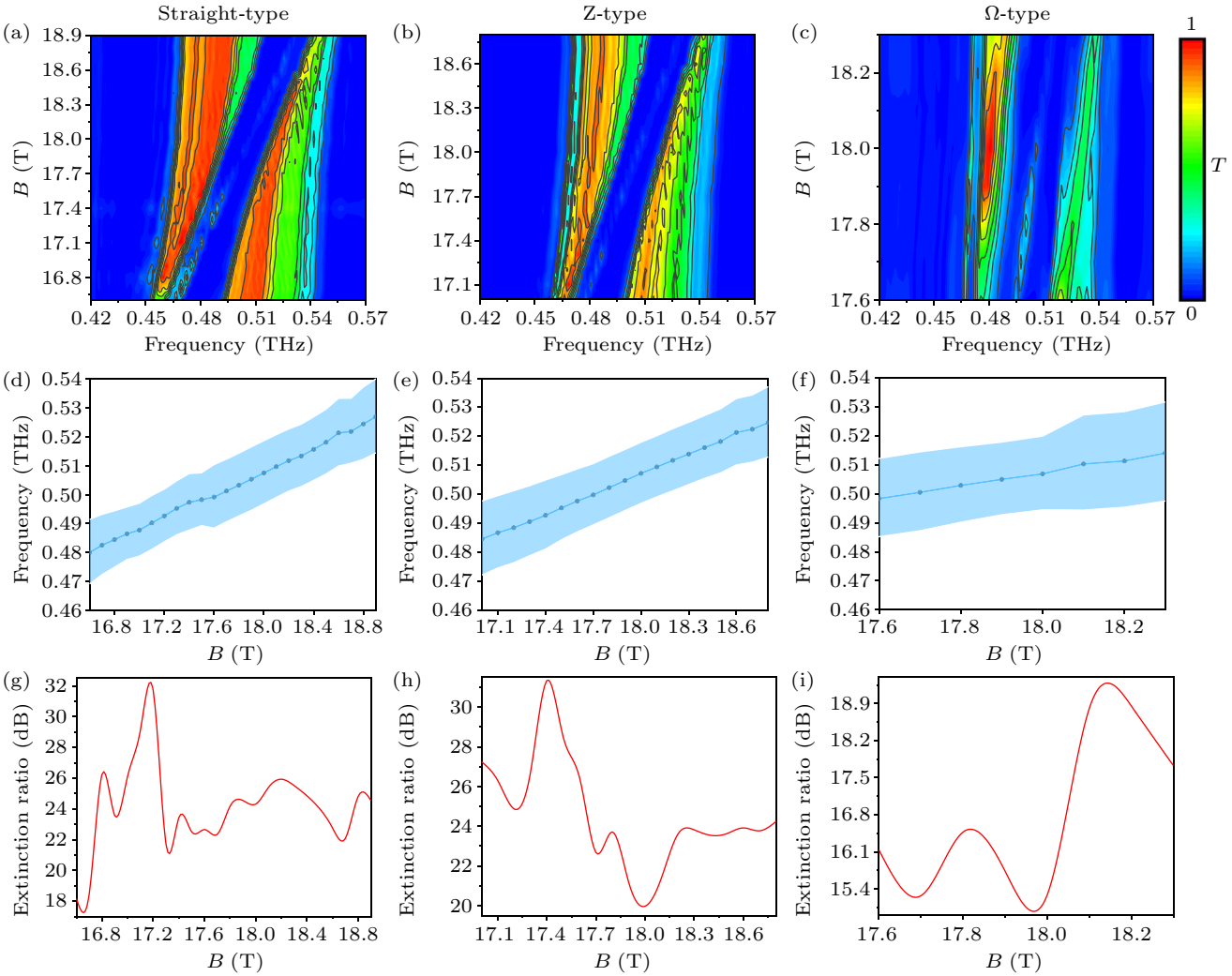


Fig. 5. Contour plots of forward transmittance spectra of the straight waveguide (a), Z-shape waveguide (b), and Ω-shape waveguide (c) under different magnetic fields. Plots of the center wavelengths of the "off" band of the straight waveguide (d), Z-waveguide (e) and Ω-waveguide (f) under different magnetic fields. Extinction ratios of the straight waveguide (g), Z-waveguide (h) and Ω-waveguide (i) under different magnetic fields.

the passband within the photonic bandgap. Meanwhile, for a zigzag-type boundary, the gap is also shifted between the bulk bands when the applied magnetic field ranges from 16.6 T to 18.9 T. In this way, the wavelength region of the "off" state within the transmittance spectrum. The resulting contour plots of the forward transmittance under different applied magnetic fields for the three waveguide structures are shown in Figs. 5(a)–5(c), respectively. As can be seen from the figures, the center wavelength of the "off" region is gradually blue-shifted with the increase of the applied magnetic field. The trends of the shifted wavelength regions are plotted in Figs. 5(d)–5(e). Due to the narrower working bandwidths of the Z- and Ω-shape waveguides compared to straight waveguides, the tuning ranges are 17 T–18.8 T and 17.6 T–18.3 T, respectively.

Extinction ratio (ER) and insertion loss (IL) are two important parameters for measuring the performance of a switch. The extinction ratio of a switch is defined as the ratio of the power in the on state to the power in the off state, expressed in logarithmic form

$$\mathrm{ER} = 10\lg\left(\frac{P_1}{P_0}\right)\ (\mathrm{dB}). \tag{5}$$

The insertion loss of a switch is defined as the ratio of the input optical power to the output optical power, expressed in logarithmic form

$$\mathrm{IL} = 10\lg\left(\frac{P_{\mathrm{in}}}{P_{\mathrm{out}}}\right)\ (\mathrm{dB}). \tag{6}$$

As a result, we can calculate the extinction ratio curves of the three waveguides corresponding to different magnetic fields as shown in Figs. 5(g)–5(i), respectively. Among them, a high extinction ratio of 31.66 dB and a low insertion loss of 0.13 dB at 0.49 THz at 17.2 T of the straight waveguide structure have been achieved, showing the high performance of our THz switches. The performance comparison of similar terahertz switches with other modulations is shown in Table S1, which can be found in supplement 1 Section 11. As one can see in the table, our THz switch has a relatively high extinction ratio and low insertion loss, with a fast response time.

5. Conclusion

In conclusion, we show a magnetically tunable THz switch based on a VPC structure. By applying an external magnetic field, the magnetic permeability of the ferrite material can be tuned to achieve switches with tunable wavelength regions being turned off. The "off" regions can be accurately controlled by the strength of the magnetic field. Meanwhile, high forward transmittance is achieved due to the unique spin–valley locking effect of VPC structures, resulting in high extinction ratios. In addition, compared with THz switches based on traditional PC waveguide structures, the performance of our topological switches is unaffected by defects, manufacturing errors and sharp corners. Therefore, it will find broad applications in THz communication. Furthermore, the design principle can be generally applied to design various functional devices in the THz region.

Acknowledgments

Project supported by the National Key Research and Development Program of China (Grant No. 2022YFA1404201), Australia Research Council (Grant Nos. DP220100603 and FT220100559), the National Natural Science Foundation of China (Grant No. U23A20375), the Natural Science Foundation of Shanxi Province (Grant No. 202403021211011), Research Project Supported by Shanxi Scholarship Council of China (Grant No. 2024-032), Fund Program for the Scientific Activities of Selected Returned Overseas Professionals in Shanxi Province (Grant No. 20240006), the Program of State Key Laboratory of Quantum Optics and Quantum Optics Devices (Grant No. KF202402), Basic Scientific Research Conditions and Major Scientific Instrument and Equipment Development of Anhui Science and Technology Department (Grant No. 2023YFF0715700), Key Research Project of Shanxi Province (Grant No. 202302150101001), and Linkage Project Scheme (Grant Nos. LP210200345 and LP210100467).

References

[1] Sheikh F, Zantah Y, Mabrouk I B, Alissa M, Barowski J, Rolfes I and Kaiser T 2021 *IEEE Trans. Antennas Propag.* **69** 7820
[2] Yang Y H, Yamagami Y, Yu X B, Pitchappa P, Webber J, Zhang B L, Fujita M, Nagatsuma T and Singh R 2020 *Nat. Photonics* **14** 446
[3] Rappaport T S, Xing Y C, Kanhere O, Ju S H, Madanayake A, Mandal S, Alkhateeb A and Trichopoulos G C 2019 *IEEE Access* **7** 78729
[4] Nagatsuma T, Ducournau G and Renaud C C 2016 *Nat. Photonics* **10** 371
[5] Li W L, Hu X M, Wu J B, Fan K B, Chen B W, Zhang C H, Hu W, Cao X, Jin B B, Lu Y Q, Chen J and Wu P H 2022 *Light-Sci. Appl.* **11** 191
[6] Luo X Q, Luo J, Hu F R and Li G Y 2023 *Chin. Phys. B* **32** 027801
[7] Han P, Wang X K and Zhang Y 2020 *Adv. Opt. Mater.* **8** 1900533
[8] Tzydynzhapov G, Gusikhin P, Muravev V, Dremin A, Nefyodov Y and Kukushkin I 2020 *J. Infrared. Millim. Te.* **41** 632
[9] Bharadwaj A N, Kashyap A M, Jayachandran R and Kishore R 2023 *International Conference on Recent Trends in Electronics and Communication (ICRTEC)*, February 10–11, 2023, Mysore, India, p. 1
[10] Liu X D, Huang J L, Chen H, Qian Z F, Ma J W, Sun X K, Fan S T and Sun Y W 2022 *Photonics Res.* **10** 1090
[11] Liu H, Chen W, Ma J, Zhang S Y, He H L, Fan Y X and Tao Z Y 2023 *Opt. Express* **31** 16303
[12] Zhang K, Zhang L, Duan D, Fan Y X and Tao Z Y 2018 *J. Lightwave Technol.* **36** 4401
[13] Wu C Y, Fan J X and Wen G H 2020 *IEEE* 3*rd International Conference on Electronic Information and Communication Technology (ICEICT)*, February 1, 2020, Shenzhen, China, p. 452
[14] Zhang Y F, Li P L, Chen Y and Han Y Q 2019 *Optik* **181** 134
[15] Zhou W, Chen H M, Ji K and Zhuang Y Y 2017 *Photonic Nanostruct.* **23** 28
[16] Li J S 2014 *Optik* **125** 3221
[17] Fan F, Guo Z, Bai J J, Wang X H and Chang S J 2011 *J. Opt. Soc. Am. B* **28** 697
[18] Sun J Z, Zhang L and Gao F 2016 *Chin. Phys. B* **25** 108701
[19] Sun J Z, Zhang L and Gao F 2016 *Optik* **127** 8096

[20] Maleki Javan A R and Granpayeh N 2008 *Opt. Quantum Electron.* **40** 695

[21] Dmitriev V, Melo G and Castro W 2021 *IEEE Trans. Magn.* **57** 2900209

[22] Dehghan M, Moravvej-Farshi M K, Jabbari M, Darvish G and Ghaffari-Miab M 2023 *J. Opt. Soc. Am. B* **40** 1773

[23] Dong R Y, Sui J Y, Li Z J and Zhang H F 2024 *Opt. Laser Technol.* **169** 110004

[24] Wu M, Fei H M, Lin H, Zhao X D, Yang Y B and Chen Z H 2021 *Acta Phys. Sin.* **70** 028501 (in Chinese)

[25] Wu M, Fei H M, Lin H, Zhao X D, Yang Y B, Liu X, Zhang M D, Cao B Z and Chen Z H 2021 *Opt. Mater.* **112** 110483

[26] Fei H M, Yan S, Xu Y C, Lin H, Wu M, Yang Y B, Chen Z H, Tian Y and Zhang Y M 2020 *Acta Phys. Sin.* **69** 184214 (in Chinese)

[27] Fei H M, Zhang Q, Wu M, Lin H, Liu X, Yang Y B, Zhang M D, Guo R and Han X T 2020 *Appl. Opt.* **59** 4416

[28] Fei H M, Yan S, Wu M, Lin H, Yang Y B, Zhang M D and Han X 2020 *Opt. Commun.* **477** 126346

[29] Fei H M, Wu M, Lin H, Yang Y B, Liu X, Zhang M D and Cao B Z 2020 *Photonic Nanostruct.* **41** 100829

[30] Fei H M, Wu M, Lin H, Liu X, Yang Y B, Zhang M D and Cao B Z 2019 *Superlatt. Microstruct.* **132** 106155

[31] Fei H, Wu M, Xu T, Lin H, Yang Y, Liu X, Zhang M and Cao B 2018 *J. Opt.* **20** 095004

[32] Sun Y W, Mei Z J, Xu X J, Xie Q X, Fan S T, Qian Z F and Liu X D 2023 *APL Photonics* **8** 110901

[33] Tan Y J, Wang W H, Kumar A and Singh R 2022 *Opt. Express* **30** 33035

[34] Kumar A, Gupta M, Pitchappa P, Wang N, Szriftgiser P, Ducournau G and Singh R 2022 *Nat. Commun.* **13** 5404

[35] Webber J, Yamagami Y, Ducournau G, Szriftgiser P, Iyoda K, Fujita M, Nagatsuma T and Singh R 2021 *J. Lightwave Technol.* **39** 7609

[36] Devi K M, Jana S and Chowdhury D R 2021 *Opt. Mater. Express* **11** 2445

[37] Wan X, Peng C Y, Li G, Yang J H and Qi X Y 2023 *Chin. Phys. B* **32** 114208

[38] Shen Y F, Xu X F, Sun M, Zhou W J and Chang Y J 2024 *Chin. Phys. B* **33** 044203

[39] Wang Y, Fei H M, Lin H, Bai J, Zhang M D, Liu X, Cao B Z, Tian Y and Xiao L T 2024 *Opt. Express* **32** 3980

[40] Bai J, Fei H M, Lin H, Wang Y, Zhang M D, Liu X, Cao B Z, Tian Y and Xiao L T 2024 *Appl. Opt.* **63** 4940

[41] Wang X R, Han Y H, Fei H M, Lin H, Zhang M D, Liu X, Cao B Z, Yang Y B, Chen Z H and Xiao L T 2023 *Opt. Express* **31** 13933

[42] Wang X R, Fei H M, Lin H, Wu M, Kang L J, Zhang M D, Liu X, Yang Y B and Xiao L T 2023 *Chin. Phys. B* **32** 074205

[43] Kang L J, Fei H M, Lin H, Wu M, Wang X R, Zhang M D, Liu X, Sun F and Chen Z H 2023 *Opt. Express* **31** 2807

[44] Wu M, Yang Y B, Fei H M, Lin H, Zhao X D, Kang L J and Xiao L T 2022 *J. Lightwave Technol.* **40** 7610

[45] Wu M, Yang Y B, Fei H M, Lin H, Han Y H, Zhao X D and Chen Z H 2022 *Opt. Express* **30** 6275

[46] Yang Q H, Zhang H W, Liu Y L, Wen Q Y and Zha J 2008 *Chin. Phys. Lett.* **25** 3957

[47] David M P 1998 *Microwave Engineering* 4th Edn. (New York: Wiley) pp. 451–493

[48] Kee C S, Kim J E, Park H Y, Park I and Lim H 2000 *Phys. Rev. B* **61** 15523

[49] Han Y H, Fei H M, Lin H, Zhang Y M, Zhang M D and Yang Y B 2021 *Opt. Commun.* **488** 126847

[50] Lu L, Joannopoulos J D and Soljačić M 2014 *Nat. Commun.* **8** 821

[51] Deng W M, Chen X D, Chen W J, Zhao F L and Dong J W 2019 *Nanophotonics* **8** 833

[52] Chen X D, Zhao F L, Chen M and Dong J W 2017 *Phys. Rev. B* **96** 020202

[53] Ezawa M 2013 *Phys. Rev. B* **88** 161406

[54] Tang G H, Hong Y L, Zhang R L, Fan R H, Ma Z L, Wu X Y, Qi D X, Peng R W and Wang M 2023 *Phys. Rev. B* **108** 205411

[55] Dong J W, Chen X D, Zhu H Y, Wang Y and Zhang X 2017 *Nat. Mater.* **16** 298

[56] Liu J W, Shi F L, He X T, Tang G J, Chen W J, Chen X D and Dong J W 2021 *Adv. Phys. X* **6** 1905546